Contents lists available at ScienceDirect

Materials Reports: Energy

Original Research Report

Introducing Ag in $Ba_{0.9}La_{0.1}FeO_{3-\delta}$: Combining cationic substitution with metal particle decoration

Alessio Belotti [a], Jiapeng Liu [a], Antonino Curcio [a], Jian Wang [b], Zheng Wang [a], Emanuele Quattrocchi [a], Mohammed B. Effat [a,1], Francesco Ciucci [a,c,*]

[a] Department of Mechanical and Aerospace Engineering, The Hong Kong University of Science and Technology, Hong Kong, China
[b] Department of Chemistry, College of Science, Seoul National University, Seoul, South Korea
[c] Department of Chemical and Biological Engineering, The Hong Kong University of Science and Technology, Hong Kong, China

ABSTRACT

$BaFeO_{3-\delta}$-derived perovskites are promising cathodes for intermediate temperature solid oxide fuel cells. The activity of these perovskites depends on the number of oxygen vacancies in their lattice, which can be tuned by cationic substitution. Our first-principle calculations show that Ag is a promising substitute for the Fe site, resulting in a reduced oxygen vacancy formation energy compared with the pristine $BaFeO_{3-\delta}$. Ag has limited solubility in perovskites, and its introduction generates an Ag metal secondary phase, which influences the cathode performances. In this work, we investigate the matter, using a $Ba_{0.9}La_{0.1}Fe_{1-x}Ag_xO_{3-\delta}$ series of materials as a case study. Acknowledging the limited solubility of Ag in $Ba_{0.9}La_{0.1}Fe_{1-x}Ag_xO_{3-\delta}$, we aim to distinguish the effects of Ag substitution from those of the Ag secondary phase. We observed that Ag substitution increases the number of oxygen vacancies, confirming our calculations, and facilitates the oxygen incorporation. However, Ag substitution lowers the number of holes, in this way reducing the electronic p-type conductivity. On the other hand, Ag metal positively affects the electronic conductivity and helps the redistribution of the electronic charge at the cathode-electrolyte interface.

1. Introduction

Solid oxide fuel cells (SOFCs) are promising energy conversion devices that may help to reduce global pollution and tackle global warming, two of the most significant challenges of this century.[1] SOFCs show higher efficiency than other fuel cell technologies: they are fuel flexible, and less affected by fuel impurities.[2] Conventional SOFCs require high temperatures, typically in the range between 800 and 1000 °C, to catalyze the oxygen reduction reaction (ORR) occurring at the cathode. These high temperatures cause long start-up times, require complex heat management systems, and narrow the range of materials that can be used for interconnects and current collectors. Conventional cathodes need high temperatures because their active reaction area is small, and

consists of the intersection of cathode, electrolyte, and gas phases.[3] The use of mixed ionic electronic conductor (MIEC) cathodes solves this issue by extending the active area to the whole cathode-gas interface. If effective MIECs are used, the operating temperatures can be reduced to the 500–800 °C range.[4] The most common MIEC cathodes are oxygen deficient perovskites with an $ABO_{3-\delta}$ formula, where the A site is an alkaline earth or lanthanide, and the B site a transition metal. Their activity is closely linked to the presence of oxygen vacancies in the lattice. Among the $ABO_{3-\delta}$ perovskites, cubic $BaFeO_{3-\delta}$ (BFO), was found to reach surprisingly high catalytic activity.[5] The cubic phase was stabilized by several groups, including ours, by La substitution.[6–10] To understand the mechanisms underpinning BFO's activity and stability, cationic substitution in the Fe site has also been studied. For example, it was

---

* Corresponding author. Department of Mechanical and Aerospace Engineering, The Hong Kong University of Science and Technology, Hong Kong, China.
E-mail address: francesco.ciucci@ust.hk (F. Ciucci).

[1] Current address: Mechanical Engineering Department, Faculty of Engineering, Assiut University, Assiut, Egypt
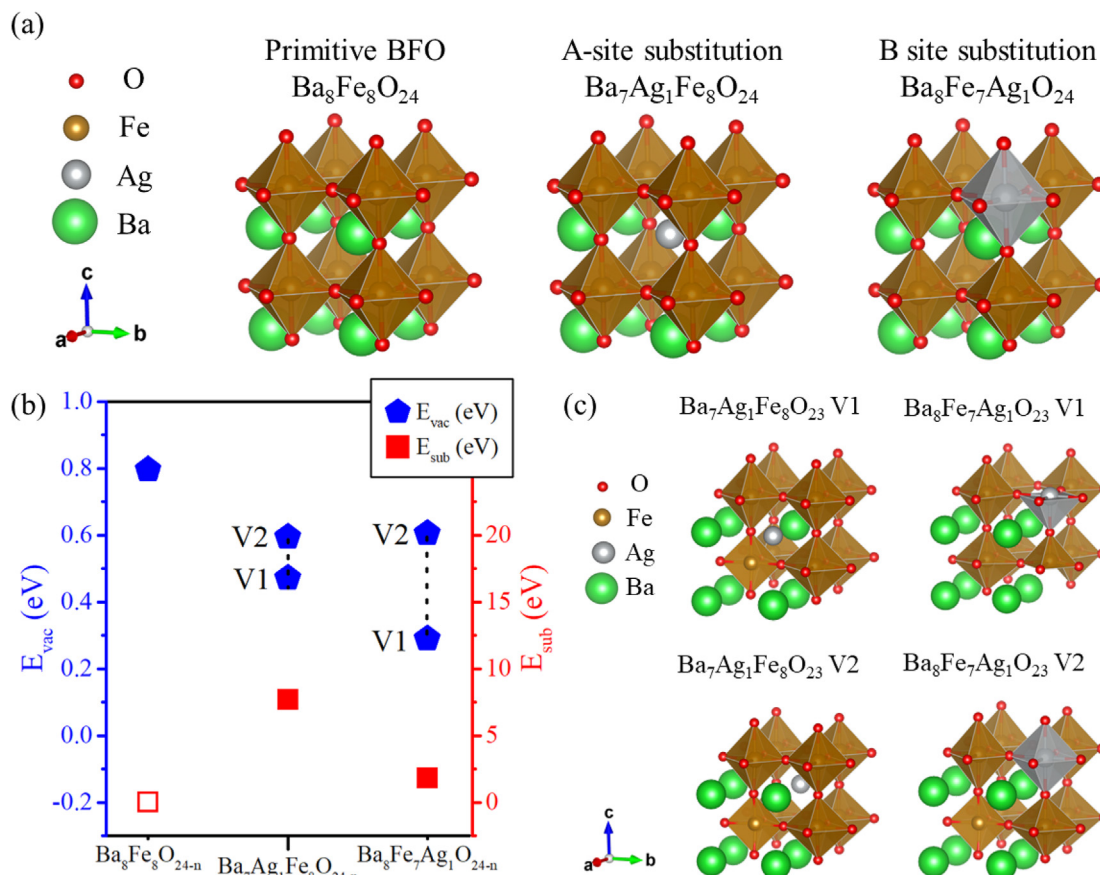
Fig. 1. (a) Relaxed structures of $Ba_8Fe_8O_{24}$, $Ba_8Fe_7Ag_1O_{24}$, and $Ba_7Ag_1Fe_8O_{24}$; (b) defect formation energy E_{sub} for Ag substitution in the A and B sites of $Ba_8Fe_8O_{24}$ and oxygen vacancy formation energies E_{vac}. (c) Relaxed oxygen vacant structures in which the vacancy is located near Ag (V1) and far from Ag (V2), respectively.

observed that Co substitution improves the performance, as in $Ba_{0.5}Sr_{0.5}Co_{0.8}Fe_{0.2}O_{3-\delta}$, because of the high redox activity of $Co^{3+/4+}$.[11] Other studies instead showed performance improvements by straining the BFO lattice with the substitution of larger ions (i.e. Ce^{4+}, Zr^{4+}, and In^{3+}) in the Fe site.[12-15] Lattice strain weakens the Fe–O bond, enhancing the formation of oxygen vacancies. Substituting BFO with a redox-active element that can also strain the lattice because of its size may result in improved activity. To achieve this, $^{VI}Ag^{+/3+}$ substitution in the $^{VI}Fe^{3+/4+}$ site (where VI is the coordination number of the cation) could be an interesting case study, since it is a redox-active element with a larger ionic radius (between 0.75 Å and 1.15 Å[16]) than the one of Fe in BFO (0.60 Å[8]). Among Ag-doped materials, promising results were observed by Zhang et al.,[17] who studied Ag substitution in $Sr_{0.95}Ag_{0.05}Co_{0.9}Nb_{0.1}O_{3-\delta}$. Then, Lim et al.[18] and Kucharczyk et al.[19] observed that $LaMnO_{3-\delta}$ and $LaFeO_{3-\delta}$ have limited solubility for Ag substitution in the A site and generate secondary Ag-rich phases. From the work of Guo et al.[20] we see that such secondary phases positively contribute to the catalysis. Finally, Zhu et al.[21] and Kim et al.[22] used Ag substitution to exsolve active Ag metal nanoparticles as an aid to the ORR catalysis. To sum up, Ag is a large, active element which can potentially dope the A site of $SrCoO_{3-\delta}$-derived perovskites. B site doping is also a promising strategy. In particular, Ag substitution in the Fe site of BFO has never been explored before. Highly Ag-doped materials reportedly generate Ag-rich secondary phases, suggesting a limited Ag solubility, and such secondary phases further improve the cathode performance. In carrying out such an investigation and understanding how these materials operate, it is important to differentiate the roles of the substitution and secondary phase in the catalysis. Firstly, we examined Ag substitution in the A and B sites of the perovskite lattice by calculating the defect formation energy. Secondly, we evaluated the impact of the Ag substitutional defect on the oxygen vacancy formation energy. The preliminary

calculations revealed a lower defect formation energy for Ag substitution in the Fe site of BFO compared to that in the Ba site. Therefore, our subsequent study focused on the Fe site and on the influence of Ag on the Fe–O bond. We then synthesized $Ba_{0.9}La_{0.1}FeO_{3-\delta}$ (BLF), $Ba_{0.9}La_{0.1}Fe_{0.95}Ag_{0.05}O_{3-\delta}$ (BLFA-5), and $Ba_{0.9}La_{0.1}Fe_{0.9}Ag_{0.1}O_{3-\delta}$ (BLFA-10), introducing La to ensure BFO's cubic phase stabilization and to balance the total charge.[6-9] To distinguish the role of Ag substitution from that of the Ag metal secondary phase, the perovskites were compared with another composite material, named BLF + A, obtained by thermo-mechanically enriching BLF with Ag metal particles as described in the experimental section. The results of the investigation indicated that Ag substitution increases the number of oxygen vacancies in the bulk material, thus enhancing the activity of the cathode. On the other hand, the Ag metal secondary phase increases the electronic conductivity of the perovskite.

2. Methods

2.1. Computational study

We conducted the first principle calculations using spin-polarized density functional theory (DFT) with the Vienna ab initio simulation package (VASP).[23,24] The simulations used the projector augmented waves method with the Perdew-Burke-Ernzerhof (PAW-PBE) exchange-correlation functional,[25] under the generalized gradient approximation (GGA) scheme[26] and DFT + U formalism.[27] The valence electrons for each element were Ba $(5s^2 5p^6 6s^2)$, Fe $(3p^6 3d^7 4s^1)$, Ag $(4d^{10} 5s^1)$ and O $(2s^2 4p^4)$. The Hubbard-U value was set at 4 eV to take into account the localization of the Fe 3d[28,29] We modeled BFO as a ferromagnetic compound consistent with the literature.[30] The energy
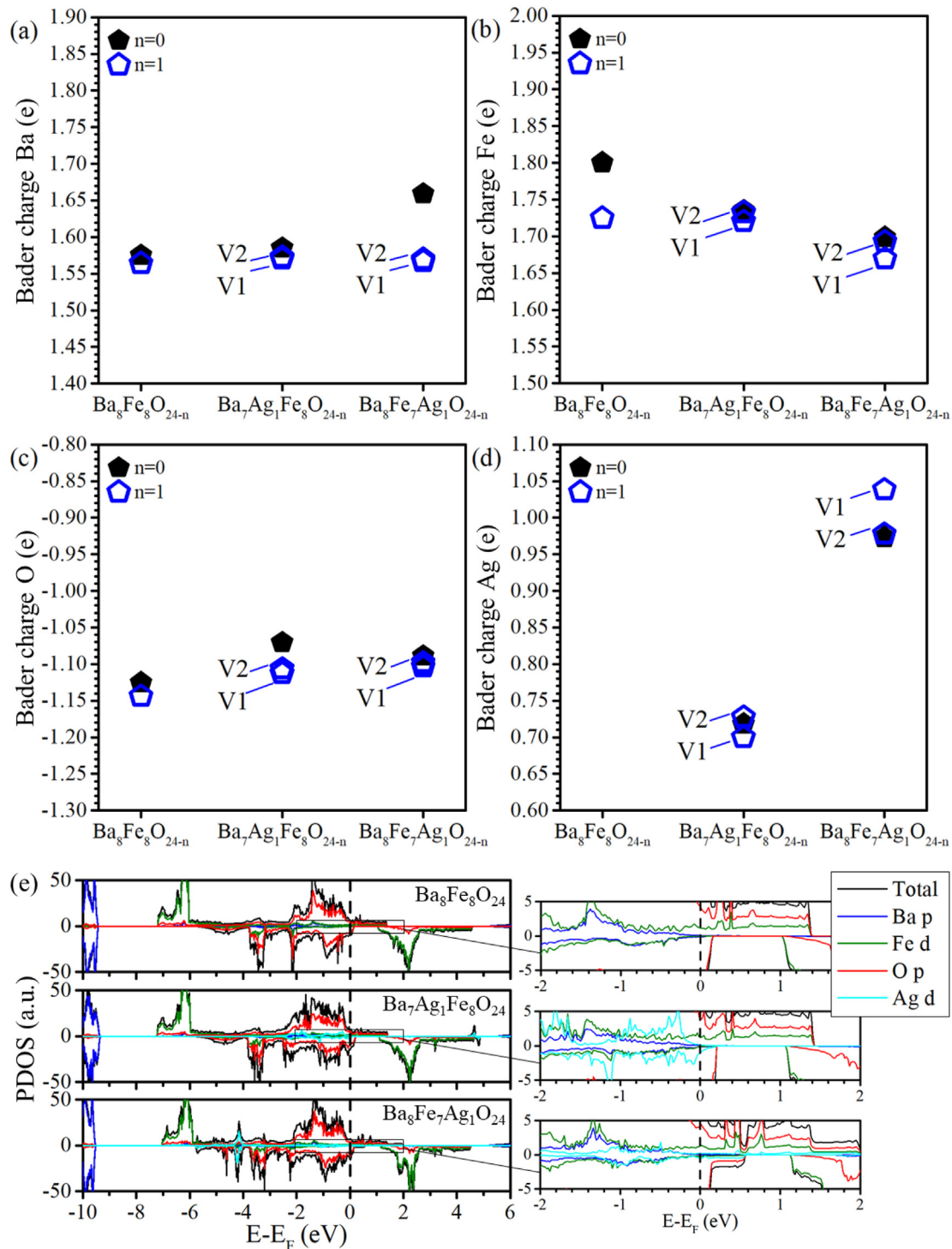
Fig. 2. Bader charge of (a) Ba, (b) Fe, (c) O, and (d) Ag in $Ba_8Fe_8O_{24-n}$, $Ba_7Ag_1Fe_8O_{24-n}$, and $Ba_8Fe_7Ag_1O_{24-n}$, respectively. (e) Comparison of the density of states in $Ba_8Fe_8O_{24}$, $Ba_8Fe_7Ag_1O_{24}$ and $Ba_7Ag_1Fe_8O_{24}$.

cutoff was set as 520 eV, and the Brillouin zone was sampled using the 6 × 6 × 6 k-points under Monkhorst–Pack algorithm. Both the lattice parameters and the positions of the atoms were allowed to change until the energy and force converged within 10^{-5} eV and 0.02 eV/Å, respectively. We constructed 2 × 2 × 2 supercells to model the materials, using the compositions $Ba_8Fe_8O_{24-n}(n = 0, 1)$, $Ba_7Ag_1Fe_8O_{24-n}(n = 0, 1)$, and $Ba_8Fe_7Ag_1O_{24-n}(n = 0, 1)$. For the O vacancy, we considered all possible arrangements relative to the position of the substituted Ag cation. The energies needed to form an Ag substitutional defect were computed as follows:

$$E_{sub-A} = E_{BAF} - E_{BF} + \mu_{Ba} - \mu_{Ag} \tag{1a}$$

$$E_{sub-B} = E_{BFA} - E_{BF} + \mu_{Fe} - \mu_{Ag} \tag{1b}$$

where E_{sub-A} and E_{sub-B} refer to Ag substitution in the A and B sites, respectively; E_{BF}, E_{BAF}, and E_{BFA} are the formation energies of the $Ba_8Fe_8O_{24}$, $Ba_7Ag_1Fe_8O_{24}$, and $Ba_8Fe_7Ag_1O_{24}$ supercells respectively; μ_{Ba}, μ_{Fe}, and μ_{Ag} are the chemical potentials of Ba (−1.92 eV), Fe (−8.46 eV), and Ag (−2.83 eV) respectively.[31] The vacancy formation energy,
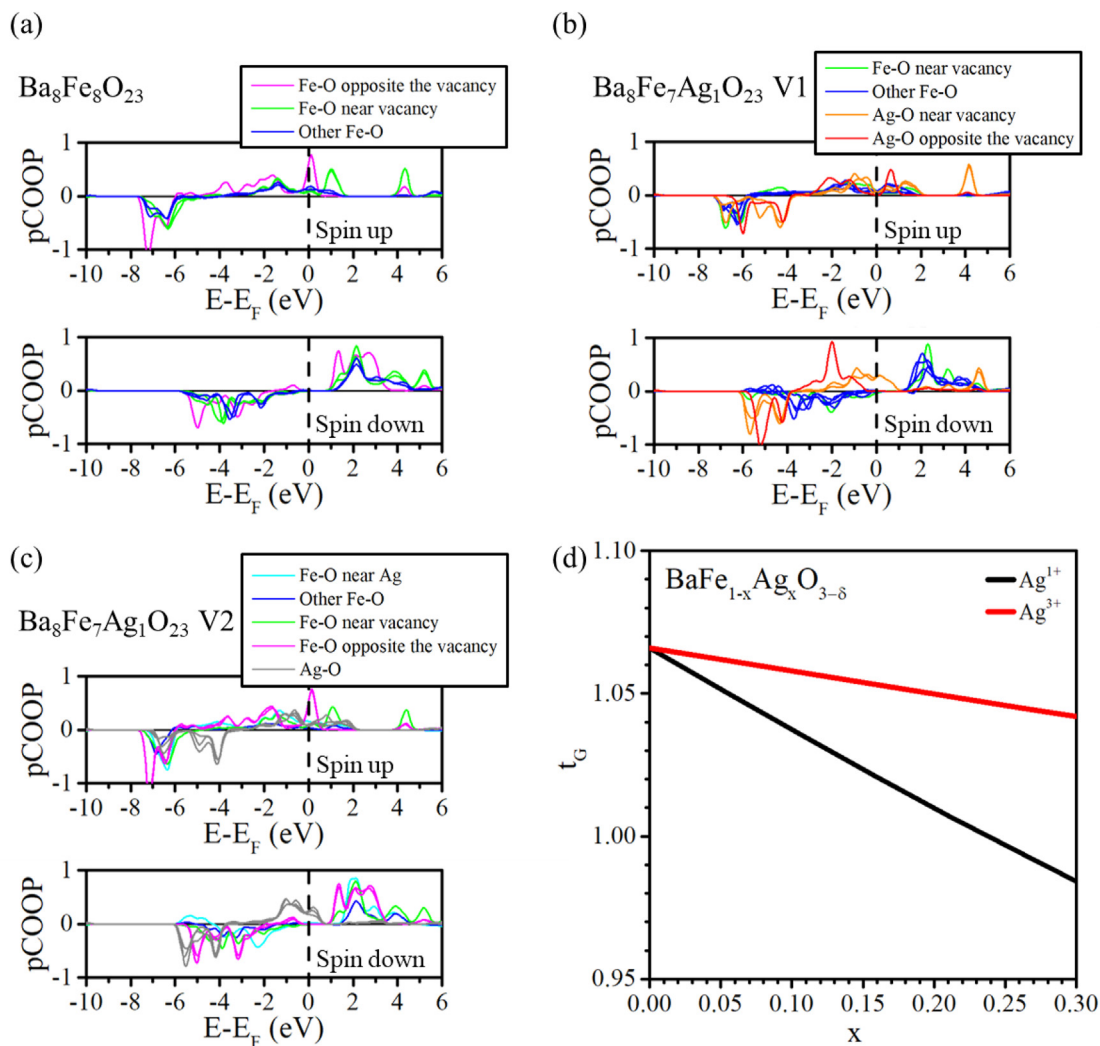
Fig. 3. (a) Projected crystal orbital overlap populations of the Ag-doped oxygen vacant structures: (a) $Ba_8Fe_8O_{23}$, (b) $Ba_8Fe_7Ag_1O_{23}$ V1 and (c) $Ba_8Fe_7Ag_1O_{24}$ V2. (d) t_G factor in $BaFe_{1-x}Ag_xO_{3-\delta}$, influence of $^{VI}Ag^+$ and $^{VI}Ag^{3+}$substitution in the $^{VI}Fe^{3+/4+}$ site.

E_{vac},[28] was calculated using the following formula:

$$E_{vac} = E_{def} - E_i + \mu_{O_2}/2 + \Delta h_O/2 \qquad (2)$$

where E_i and E_{def} are the energies of the original supercell and the supercell with one oxygen vacancy, respectively; Δh_O is the O_2 over-binding correction term (1.36 eV[32]); and μ_{O_2} is the chemical potential of a O_2 molecule (-9.86 eV). The analysis was completed by calculating the Bader charge and the projected density of states (pDOS). Finally, the projected crystal orbital overlap population (pCOOP) of the single bonds was extracted from the plane-wave based DFT by combining the VASP package with the local orbital basis suite towards electronic-structure reconstruction (LOBSTER) package.[33–36]

2.2. Material synthesis

We prepared the BLF, BLFA-5, and BLFA-10 materials using a sol-gel complexing process. Ethylenediamine-tetraacetic acid (EDTA) and citric acid (CA) were used as chelating agents.[37,38] Firstly, stoichiometric amounts of the nitrates $Ba(NO_3)_2$ (Sigma Aldrich, $\geq$ 99%), $La(NO_3)_3$ (Sigma Aldrich, $\geq$ 99.9%), $Fe(NO_3)_3 \cdot 9H_2O$ (Sigma Aldrich, $\geq$ 98%), and $AgNO_3$(Sigma-Aldrich, $\geq$ 99.0%) were dissolved in deionized water. Then, EDTA and CA were added as chelating agents, following a molar ratio of 1:1:2, respectively. Ammonia was added to adjust the pH level of

the solution to 6. The solution was then heated on a hot plate at 120 °C and stirred at 120 rpm until the water completely evaporated. The remaining gel was pre-calcined at 250 °C for 6 h and calcined at 1000 °C for 12 h in a high-temperature furnace, using a ramping rate of 10 °C/min. Finally, half of the BLF prepared was ball-milled with Ag_2O at a molar ratio of 20:1 for 4 h, generating the composite material BLF + A.

2.3. Physical characterizations

We examined the phases of the synthesized materials by X-ray diffraction (XRD) and high-temperature XRD (HT-XRD), using an Empyrean XRD diffractometer (Malvern PANanalytical) with filtered Cu K-alpha radiation ($\lambda = 1.5406$ Å, 40 kV, 40 mA) in the range from $2\theta = 10°$ to $90°$. The HT-XRD measurements were conducted between room temperature (RT) and 900 °C, with increments of 100 °C. The XRD patterns were fitted using Rietveld refinement (PDF#14–0180). The composition of the bulk was examined by X-ray fluorescence (XRF), using the element analyzer JEOL JSX-3201Z. We also studied the surface of the materials with the X-ray photoelectron spectroscopy (XPS), using a Kratos Axis Ultra DLD with an Al monochromatic X-ray source. The scanning range covered to evaluate the composition of the surface was from 0 eV to 1400 eV with increments of 1 eV. The oxidation state of Ag was studied in the 360 eV and 380 eV range where the increments were set at 0.1 eV. Similar settings were used for Fe within 700 eV and 740 eV.
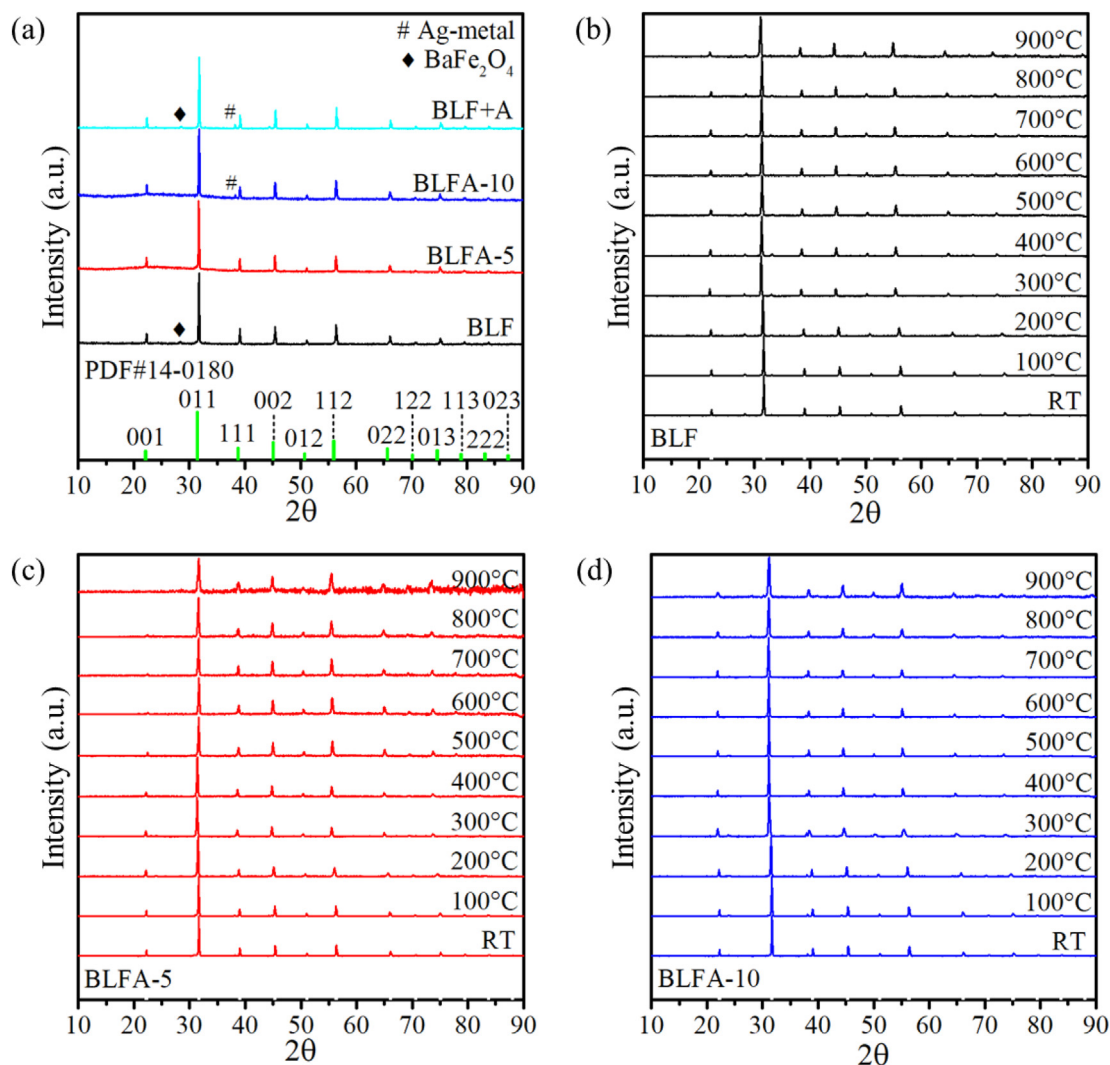
Fig. 4. (a) Room temperature XRD patterns of BLF, BLFA-5, BLFA-10, BLF + A. Reference peak positions and secondary phases are also shown. HT-XRD patterns from room temperature to 900 °C for (b) BLF, (c) BLFA-5, and (d) BLFA-10.

Table 1

Structure, lattice parameter, and secondary phases for each stoichiometry, calculated from the XRD spectra at room temperature.

Material	Structure	Lattice parameter (Å)	Secondary phases
$Ba_{0.9}La_{0.1}FeO_{3-\delta}$	$Pm\overline{3}m$	4.00	$BaFe_2O_4$
$Ba_{0.9}La_{0.1}Fe_{0.95}Ag_{0.05}O_{3-\delta}$	$Pm\overline{3}m$	4.00	N/A
$Ba_{0.9}La_{0.1}Fe_{0.9}Ag_{0.1}O_{3-\delta}$	$Pm\overline{3}m$	3.99	Ag metal
$Ba_{0.9}La_{0.1}FeO_{3-\delta} + Ag_{0.1}$	$Pm\overline{3}m$	4.00	$BaFe_2O_4$, Ag metal

From the XPS data, we also determined the concentrations of Ba and La on the surface relative to the bulk by using the surface concentration indexes (SCI_{Ba} and SCI_{Ba+La}), defined as follows:

$$SCI_{Ba} = \left[Ba_{surf}\right]/\left[Ba_{bulk}\right] - 1 \tag{3a}$$

$$SCI_{Ba+La} = \frac{\left[Ba_{surf}\right] + \left[La_{surf}\right]}{\left[Ba_{bulk}\right] + \left[La_{bulk}\right]} - 1 \tag{3b}$$

where $\left[Ba_{surf}\right]$ and $\left[La_{surf}\right]$ are the molar concentrations of Ba and La on the surface measured by XPS, $\left[Ba_{bulk}\right]$ and $\left[La_{bulk}\right]$ are the molar concentrations of Ba and La in the bulk as measured by XRF.

The bulk oxygen non-stoichiometry was measured by iodometric titration. In this process, 0.05 g of the perovskite were dissolved in a solution of deionized water with 6 M HCl and then mixed with 1.5 g of KI. I_2 was therefore generated by the following reactions

$$Ag^{3+} + 2\,I^- \rightarrow Ag^+ + I_2 \tag{4a}$$

$$Fe^{y+} + (y-2)I^- \rightarrow Fe^{2+} + \frac{y-2}{2}I_2. \tag{4b}$$

I_2 was removed by the introduction of a known amount of $Na_2S_2O_3$, using starch as an indicator, in the following reaction:

$$I_2 + 2Na_2S_2O_3 \rightarrow 2NaI + Na_2S_4O_6 \tag{5}$$

From the amount of $Na_2S_2O_3$ used to complete the reaction, we calculated the average oxidation number in the B site and the corresponding oxygen non-stoichiometry δ.

2.4. Electrochemical impedance spectroscopy

We conducted a series of impedance tests on the electrolyte-supported symmetrical cells. The electrolyte consisted of a disk prepared using 0.3 g of 20% Sm-doped ceria powder (Fuelcellsmaterials, SDC20-M). We first pressed the SDC20-M powder into pellets (area = 1.1

Table 2
Thermal expansion coefficients, derived from HT-XRD.

Material	Temperature Range	TEC ($°C^{-1}$)
$Ba_{0.9}La_{0.1}FeO_{3-\delta}$	20–100 °C	1.88×10^{-5}
	100–200 °C	5.29×10^{-5}
	200–300 °C	1.13×10^{-4}
	300–400 °C	1.89×10^{-5}
	400–500 °C	2.28×10^{-5}
	500–600 °C	1.44×10^{-5}
	600–700 °C	1.64×10^{-5}
	700–800 °C	2.37×10^{-5}
	800–900 °C	3.24×10^{-5}
$Ba_{0.9}La_{0.1}Fe_{0.95}Ag_{0.05}O_{3-\delta}$	20–100 °C	1.88×10^{-5}
	100–200 °C	5.90×10^{-5}
	200–300 °C	1.25×10^{-4}
	300–400 °C	1.08×10^{-5}
	400–500 °C	3.77×10^{-5}
	500–600 °C	2.83×10^{-5}
	600–700 °C	1.02×10^{-5}
	700–800 °C	3.89×10^{-6}
	800–900 °C	3.72×10^{-5}
$Ba_{0.9}La_{0.1}Fe_{0.9}Ag_{0.1}O_{3-\delta}$	20–100 °C	1.72×10^{-5}
	100–200 °C	4.70×10^{-5}
	200–300 °C	1.22×10^{-4}
	300–400 °C	3.12×10^{-5}
	400–500 °C	2.01×10^{-5}
	500–600 °C	1.20×10^{-5}
	600–700 °C	1.29×10^{-5}
	700–800 °C	1.66×10^{-5}
	800–900 °C	2.70×10^{-5}

Table 3
Cationic compositions, measured in the bulk by XRF and on the surface by XPS.

Element	Nominal composition (%)	XRF composition (bulk) (%)	XPS composition (near-surface) (%)
$Ba_{0.9}La_{0.1}FeO_{3-\delta}$			
Ba	45.00	42.12	42.75
La	5.00	3.07	14.82
Fe	50.00	54.82	42.43
Ag	–	–	–
$Ba_{0.9}La_{0.1}Fe_{0.95}Ag_{0.05}O_{3-\delta}$			
Ba	45.00	43.30	46.66
La	5.00	2.97	7.25
Fe	47.50	52.15	45.03
Ag	2.50	1.80	1.05
$Ba_{0.9}La_{0.1}Fe_{0.9}Ag_{0.1}O_{3-\delta}$			
Ba	45.00	43.66	62.07
La	5.00	3.15	10.72
Fe	45.00	49.81	25.67
Ag	5.00	3.80	1.53

cm^2; thickness = 0.3 mm), which we subsequently sintered at 1400 °C. The electrolytes were then coated with the cathode slurries. To prepare the slurries, we ball-milled 1.0 g of the corresponding cathode material (BLFA-0, BLFA-5, BLFA10, and BLF + A) with isopropanol (10 mL), ethylene glycol (2 mL), and glycerol (0.6 mL) for 4 h. Then, the slurries were ultra-sonicated for 1 h and spray-coated on both sides of the electrolyte. The obtained symmetric cells were sintered at 1000 °C for 2 h to remove organic residuals and ensure adhesion between the two materials. After the EIS tests, the thickness of the cathode (>10 μm) was measured by SEM. Finally, a thin layer of current collector made of Ag paste (DAD-87, Shanghai Research Institute of Synthetic Resins) was painted on both sides of the cells and cured at 180 °C for 1 h. The EIS data was collected using a VSP potentiostat (BioLogic) in the frequency range from 20 kHz to 100 mHz and a spacing of 15 points per decade. The tests were conducted by positioning the cell inside a testing chamber where both the temperature, T, and the gas atmosphere, consisting of a mixture

of dry N_2 and O_2 (purity $\geq$ 99.996%), were controlled. The oxygen partial pressure (pO_2) was set to 21%, whereas the temperature was initially raised to 700 °C and then decreased to 500 °C with decrements of 50 °C. At each temperature step, the impedance spectra were recorded at five different pO_2 (21%, 40%, 60%, 80%, 100%). From the EIS data, we calculated the area-specific resistance (ASR) from the polarization resistance[39] and the area of the cathode. We also fit the same EIS data using an equivalent circuit model (ECM) consisting in an inductance L, an Ohmic resistance $R\infty$, and two ZARCs elements in series. Then, based on the elements in the ECM, we computed an analog of the distribution of relaxation times (DRT)[40–42] to assess how the system's timescales depend on temperature and the oxygen partial pressure.

2.5. Setup for conductivity measurements

The electrical conductivity (EC) and the electrical conductivity relaxation (ECR) were measured on cuboid pellets with dimensions of 20 mm × 6 mm × 3 mm. The cuboids were prepared by isostatically pressing the BLF, BLFA-5, BLFA-10, and BLF + A powders at 300 bar into pellets, which were then sintered at 1000 °C. In both EC and ECR tests, the pellets were connected to the VSP potentiostat by four silver wires in a four-probe configuration. The tests were carried out in the same testing chamber used for the EIS. The EC was measured at pO_2 = 21%. The temperature of the furnace was initially set at 700 °C and then lowered to 300 °C, with decrements of 10 °C. At each temperature, we recorded the conductivity over time, $\sigma = \sigma(T, t)$ until its value was stabilized. The ECR tests were carried out on the same type of samples. During the ECR test the temperature of the chamber was kept constant and the pO_2 changed. The ECR response was investigated at temperatures ranging from 500 °C to 700 °C, with increments of 50 °C. While recording the conductivity $\sigma(t)$ at every time step t, the sample was kept at the initial conditions of pO_2 = 50% until completely relaxed. Then, the pO_2 of the chamber was suddenly dropped to 21%, triggering a relaxation towards a new equilibrium.[43] Since the oxygen content in the perovskite influences the electronic conductivity, we used the conductivity transient between the initial and the final states to investigate the ORR kinetics. We first normalized $\sigma(t)$ to a value σ_n between 0 and 1 such that

$$\sigma_n(t) = \frac{\sigma(t) - \sigma_i}{\sigma_\infty - \sigma_i} \tag{6}$$

where $\sigma(t)$ is the conductivity at the time step t, σ_i is the conductivity of the relaxed sample at the initial conditions and σ_∞ is the conductivity at the final state. We then fitted $\sigma_n(t)$ with the ECRTOOLS package,[44] obtaining the ORR constants of surface reaction (k_{chem}) and chemical diffusivity (D_{chem}) in their respective confidence intervals.[43]

3. Results and discussion

3.1. Computational study

As a first step, we computed the defect formation energy in both the A and B sites. To do that, Ag cations were substituted into both Ba and Fe sites of $Ba_8Fe_8O_{24-n}$, forming $Ba_7Ag_1Fe_8O_{24-n}$ and $Ba_8Fe_7Ag_1O_{24-n}$, respectively. Then, the obtained structures were relaxed (Fig. 1a). The defect formation energies (see Fig. 1b) show that E_{sub-B}1.85 eV) is lower than E_{sub-A}(7.50 eV), suggesting that Ag is most likely to be substituted in the B site of BFO. We also notice that the E_{vac} (Fig. 1b) calculated for both $Ba_7Ag_1Fe_8O_{24-n}$ and $Ba_8Fe_7Ag_1O_{24-n}$ are lower than the E_{vac} of $Ba_8Fe_8O_{24-n}$, suggesting that the presence of Ag enhances the formation of oxygen vacancies. Particularly, in the supercells with an oxygen vacancy close to Ag (V1), E_{vac} is lower than in the cells with an oxygen vacancy far from Ag (V2), see Fig. 1b and c. This indicates that oxygen vacancies are prone to locate near the Ag cation. Bader charge was calculated to study the influence of Ag doping on the electronic structure. Although Ag doping does not produce relevant changes to the charge of
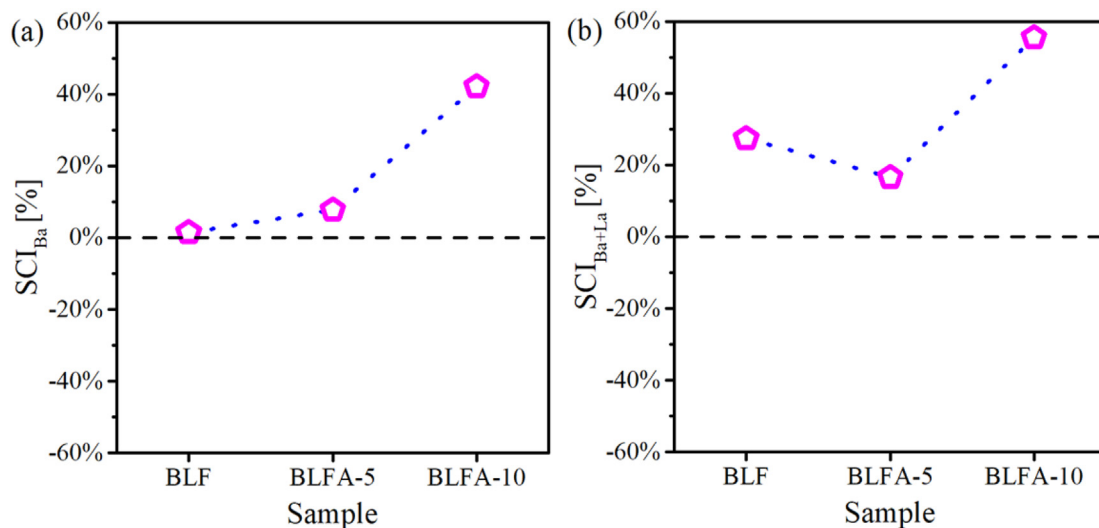
Fig. 5. Surface concentration indexes of (a) Ba and (b) Ba + La on the surface of BLF, BLFA-5, and BLFA-10 as defined in Section 2.3.
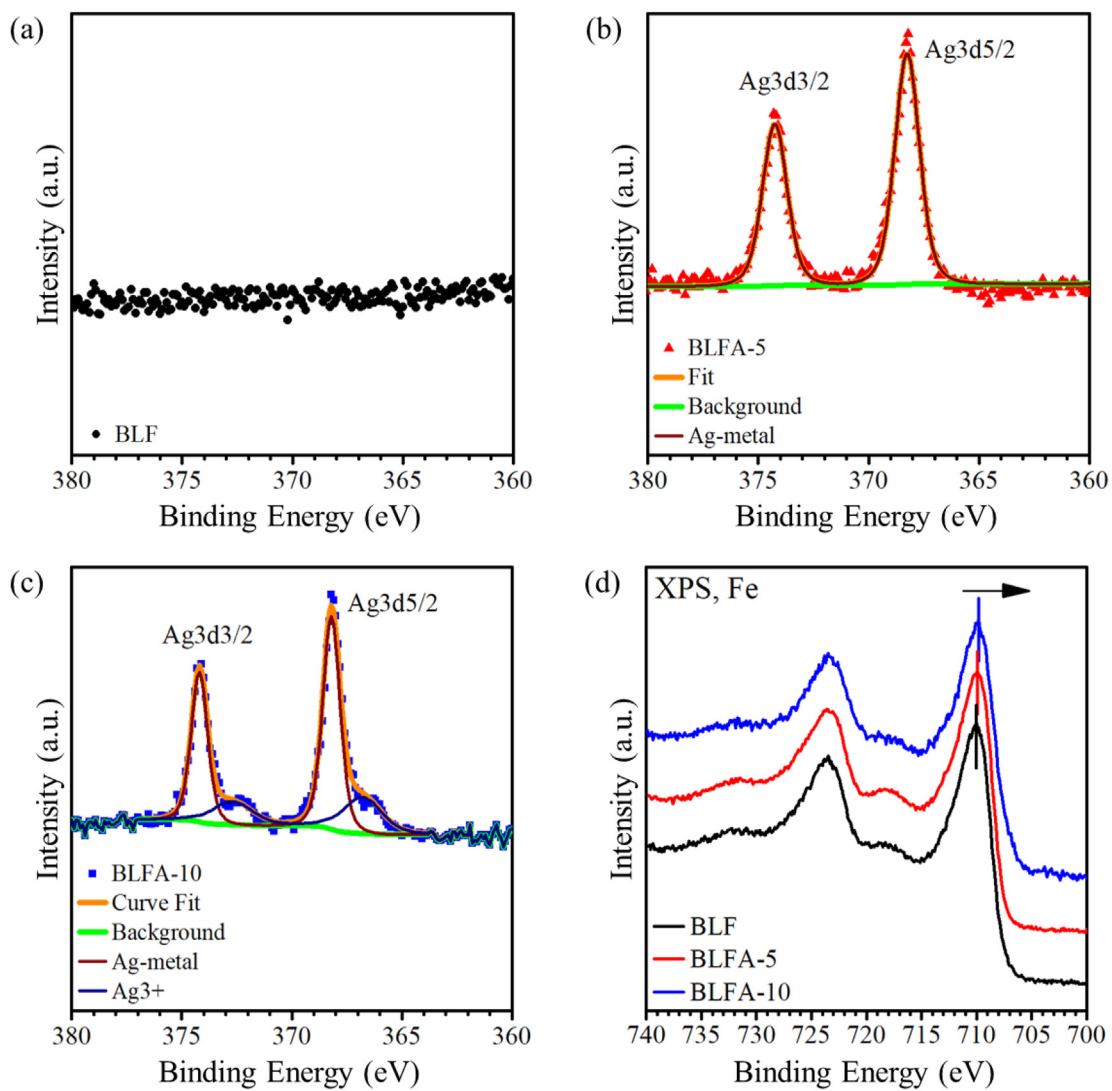

Fig. 6. XPS spectra for Ag in (a) BLF and the cationic substituted (b) BLFA-5 and (c) BLFA-10. (d) Comparison between the XPS spectra for Fe 2p in BLF (710 eV), BLFA-5 (709.9 eV), and BLFA-10 (709.8 eV), in which a right shift is observed.

Table 4

Oxygen deficiency δ for each material, measured by iodometric titration. Fe average oxidation number measured in the bulk by iodometric titration. Fe average oxidation number measured on the surface by XPS fit.

Material	δ	Oxidation state of Fe	
		Titration	XPS
$Ba_{0.9}La_{0.1}FeO_{3-\delta}$	0.37	3.15	3.24
$Ba_{0.9}La_{0.1}Fe_{0.95}Ag_{0.05}O_{3-\delta}$	0.42	3.07	3.20
$Ba_{0.9}La_{0.1}Fe_{0.9}Ag_{0.1}O_{3-\delta}$	0.47	2.95	3.09

Ba (see Fig. 2a), we observed that it lowers the Fe charge instead, especially in $Ba_8Fe_7Ag_1O_{24-n}$ (see Fig. 2b). This suggests a reduction of the number of available holes, which are responsible for the electronic conductivity (p-type). Hence, we may expect the electronic conductivity to decrease. In addition, the introduction of Ag causes less negative Bader charge of O, corresponding to a higher tendency to form oxygen vacancies, see Fig. 2c. It is also observed that the Bader charge of O in the oxygen-vacant materials is more negative, as a consequence of charge redistribution in a lower number of oxygen atoms. Finally, in Fig. 2d, we can see that the Bader charge of Ag is much higher when Ag is doped into the B-site compared to the A-site, suggesting a different oxidation state, i.e. Ag^+ in the A-site and Ag^{3+} in the B-site. This is because Ag–O bond is longer in A-site substituted BFO than B-site substituted BFO, and orbital interactions between Ag and O in the A-site is accordingly weaker than that in the B-site. As a result, the energy rise of d orbitals of Ag in the A-site is smaller than that of Ag in the B-site upon the interactions between Ag and O. Hence, Ag at the B-site would easily release electrons to become Ag^{3+}, while Ag in the A-site can still stay in a lower valence. The study of the projected density of states (pDOS), see Fig. 2e and Fig. S1, did not provide sufficient insights on the electronic structure of the material. Therefore, a more specific study of the pCOOP of each bond was carried out, observing the effects of Ag introduction and oxygen vacancy introduction on Fe–O and Ag–O bond orbitals (Fig. 3). Comparing the spin-down spectra of the bonds in $Ba_8Fe_8O_{23}$, $Ba_8Fe_7Ag_1O_{23}$(V1), and $Ba_8Fe_7Ag_1O_{23}$(V2), we can see that Ag–O partially occupies the antibonding orbitals. This is supposed to decrease the bond order of the Ag–O bond, thus its bond strength. Ag's presence generates antibonding orbitals in Fe–O too, leading to a weaker Fe–O bond. We conclude that Ag–O bond is weak and Ag introduction weakens Fe–O bonds in the structure, boosting the formation of oxygen vacancies. In addition, the pCOOP of Ag–O located opposite the oxygen vacancy (Fig. 3b, in red) exhibits notable antibonding features, making very likely the formation of another oxygen vacancy in that same position. The above observations suggest that Ag atoms may behave as a pathway for oxygen vacancy transfer through $Ba_8Fe_7Ag_1O_{23}$. Finally, we calculated the Goldschmidt tolerance factor $t_G = (r_A + r_O)/\sqrt{2}(r_B + r_O)$ of $BaFe_{1-x}Ag_xO_{3-\delta}$, where r_A is the average of ionic radii in A site, r_B is the average of ionic radii in B site, and r_O is the radius of oxygen. The ionic radii depend on the coordination and oxidation numbers of the element, i.e., $r[^{XII}Ba^{2+}] = 1.61$ Å, $r[^{VI}O^{2-}] = 1.4$ Å, $r[^{VI}Ag^+] = 1.15$ Å, $r[^{VI}Ag^{3+}] = 0.75$ Å.[16] In addition, $r[^{VI}Fe^{3+/4+}] = 0.60$ Å, was from the work of Kida et al.[8] on BFO. Ag introduction improves the cubic phase stability by lowering t_G (see Fig. 3d), but it is not enough to stabilize it at room temperature. Therefore, as anticipated in the introduction, the cubic phase was ensured by La substitution in the A site.

3.2. Structure

The XRD patterns, reported in Fig. 4a, show that the cubic phase $Pm\bar{3}m$ is reached by the four types of materials. In the BLF, we detected a small $BaFe_2O_4$ impurity, which was also identified as an impurity by Dong et al.[7] We also detected the presence of the Ag metal in both BLFA-10 and BLF + A, see reflection at 38.2°.[45] Such a peak is

consistently visible in the XRD patterns in the works of other groups on Ag substituted cubic perovskites, such as $La_{1-x}Ag_xMnO_3$ ($x > 0.1$) and $La_{1-x}Ag_xFeO_3$ ($x > 0.05$)'s ones.[18,19] The presence of Ag metal indicates that Ag's solubility in BLF is limited. We did not detect any Ag_2O or AgO secondary phases, as they are known to turn into Ag metal at temperatures above 195 °C. The space group and dimensions of perovskite's primitive cell are reported in Table 1 together with the secondary phases detected. HT-XRD analysis (Fig. 4) shows that the $Pm\bar{3}m$ phase is stable in the whole intermediate temperature range (500–800 °C). A sharp increase in the lattice parameter can also be observed above 300 °C (Fig. S3). Such an increase is due to both thermal dilation and the formation of oxygen vacancies,[12] leading to average thermal expansion coefficients (TECs) of 3.48×10^{-5} K^{-1}, 3.67×10^{-5} K^{-1}, and 3.40×10^{-5} K^{-1}, for BLF, BLFA-5, and BLFA-10, respectively (Table 2).

3.3. Surface study

Table 3 shows the compositions of the perovskite bulk (measured by XRF) and surface (measured by XPS), see also Fig. S4. The two compositions allow the computation of the indices (Fig. 5) defined by (3). We can notice that, while SCI_{Ba} and SCI_{Ba+La} are negligible in BLFA-5, they become severe in BLFA-10. Analyzing the XPS of Ag (Fig. 6) in BLFA-5, we observe a peak at a binding energy close to the ones of Ag^0 and Ag^+, in 368.3 eV and 368.6 eV, respectively.[46] Since their binding energies are too close to be distinguished, it is not possible to estimate how much Ag entered the perovskite and how it leads to the secondary phase. On the other hand, we also detected the presence of Ag^{3+} in BLFA-10, consisting of about 25% of the total amount of Ag in the spectrum. Ag^{3+} is distinguishable from the other two since its binding energy peaks at 366.8 eV.[47] This is interesting since BLFA-10 substitutes the highest amount of $Fe^{3+/4+}$ and suggests that Ag^{3+} may be present due to charge compensation. Comparing the XPSs in the scan range of Fe (Fig. 6d), we can observe the incremental right shift of the Fe 2p peaks for BLFA-5 and BLFA-10. Due to the structure of BFO-like materials, the formation of Fe^{2+} is unlikely.[48] Therefore, the shift should be caused by an increase of Fe^{3+} at the expense of Fe^{4+}.[13] The XPS of non-pure Fe oxides is affected by several spectral overlaps and multiplet splitting. Hence, the exact resolution of its chemical states is characterized by an inherent degree of error.[49] In this work, we assigned the peak values of 710 eV and 713 eV, respectively, to the 2p orbitals of Fe^{3+} and Fe^{4+}. By observing the resulting fit, we find the increase of Fe^{3+} and the decrease of Fe^{4+} (Fig. S5). This reduction of Fe 2p valence state suggests an increased concentration of oxygen vacancies near the surface, after the introduction of Ag. Similarly, the iodometric titration shows an increase of the number of oxygen vacancies in the bulk of BLFA-5 and BLFA-10 (Table 4). This is consistent with our calculations and demonstrates a higher activity of the Ag-doped materials.

3.4. Electrochemical impedance spectroscopy

The R_p obtained by EIS, i.e. the arc, can be used as a proxy of the catalytic activity. R_p depends on several kinetic steps, taking place either at the cathode-electrolyte interface, in the bulk material, or at the cathode-gas interface. We expect that Ag substitution and the Ag metal secondary phase influence different kinetic steps. Hence, we compared the EIS outcomes to differentiate the two contributions. Comparing BLF and BLF + A in Fig. 7a, we observe that the arc of BLF + A is smaller, underlining that the presence of Ag metal improves the activity. As noted by Choi et al.,[50] this improvement may be attributed to the electronic charge redistribution at the electrolyte-cathode interface, facilitated by Ag metal. It can be asserted that Ag metal catalyzes the ORR independently from BLFA-x.[51] However, it can be argued that this contribution is negligible, having Ag metal a larger ASR (between 0.92 and 3.55 Ω cm^2 at 650 °C[52]) than the one of BLF ($ASR = 0.65$ Ω cm^2 at 650 °C, see Fig. 7).
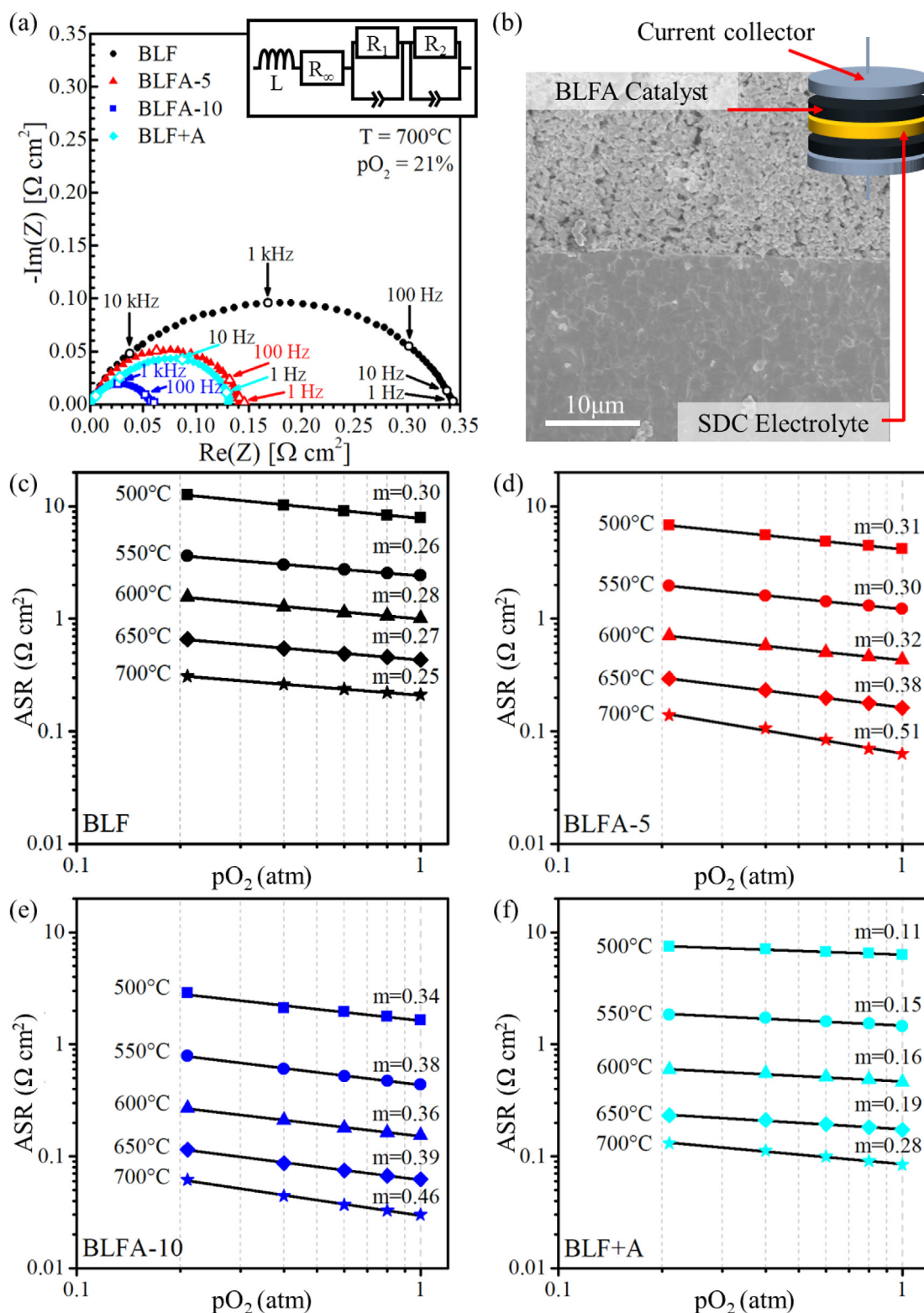
Fig. 7. (a) EIS spectra at $T = 700\ ^{\circ}C$ and $pO_2 = 21\%$ of BLF, BLFA-5, BLFA-10, BLF + A. (b) Schematics of the cell and SEM image of the interface BLFA|SDC of one symmetric cell. Area-specific resistance (ASR) of the symmetric cells (c) BLF||SDC||BLF, (d) BLFA-5||SDC||BLFA-5, (e) BLFA-10||SDC||BLFA-10, (f) BLF + A||SDC|| BLF + A at different conditions of pO_2, and temperatures.

In addition, for the small amount of Ag metal present (<5%), independent ORR catalysis would not have a noticeable influence on BLF + A's catalytic properties. In Subsections 3.5 and 3.6, we further clarify the matter by observing the influence of Ag metal on both the electric

conductivity and ECR. Comparing BLF + A with BLFA-10, which contain the same amount of Ag, we can appreciate the contribution of Ag substitution as shown by the computations. The EIS arc of BLFA-10 is smaller than that of BLF + A, suggesting that Ag substitution improves the
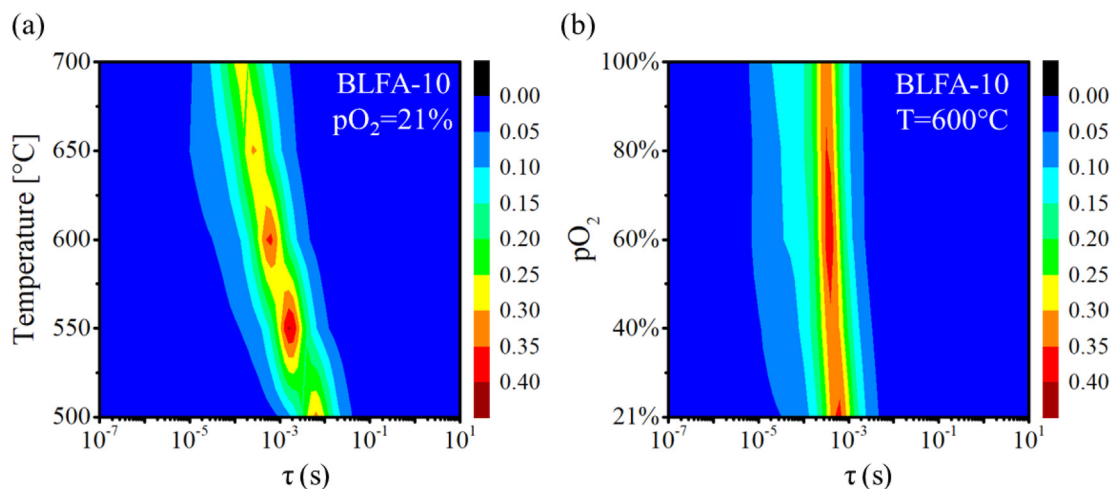
Fig. 8. DRT (normalized with respect to $R_{tot} = R_1 + R_2$) of BLFA-10 versus (a) temperature and (b) pO_2.

Table 5
Parameters of the ZARC elements in the ECM at $T = 600\ °C$ and $pO_2 = 21\%$.

Material	R_1 ($\Omega \cdot cm^2$)	R_2 ($\Omega \cdot cm^2$)	τ_1 (s)	τ_2 (s)	ϕ_1 (-)	ϕ_2 (-)
$Ba_{0.9}La_{0.1}FeO_{3-\delta}$	1.25	0.59	$1.37 \cdot 10^{-3}$	$5.34 \cdot 10^{-5}$	0.77	0.52
$Ba_{0.9}La_{0.1}Fe_{0.95}Ag_{0.05}O_{3-\delta}$	0.43	0.32	$9.69 \cdot 10^{-4}$	$1.94 \cdot 10^{-4}$	0.82	0.62
$Ba_{0.9}La_{0.1}Fe_{0.9}Ag_{0.1}O_{3-\delta}$	0.24	0.06	$6.05 \cdot 10^{-4}$	$1.75 \cdot 10^{-5}$	0.78	0.52
$Ba_{0.9}La_{0.1}FeO_{3-\delta} + Ag_{0.1}$	0.40	0.22	$6.08 \cdot 10^{-2}$	$6.35 \cdot 10^{-3}$	0.89	0.50

activity of the perovskite. In addition, as both the DFT and iodometric titration pointed out, Ag substitution lowers the vacancy formation energy. Hence, we attribute this activity improvement to the higher number of oxygen vacancies of BLFA-10. Finally, the R_p of BLFA-5 is reasonable at an intermediate value between those of BLF and BLFA-10. Then the *ASRs* at all the T and pO_2 indicated were calculated (see Fig. 7). As shown in Fig. 7, the trends above are well maintained at all the working conditions. We can also indicate the fitted exponential factors m, which link the ASR and pO_2 according to the relation

$$ASR \propto pO_2^{-m} \tag{10}$$

As shown in the work of Escudero et al.,[53] specific ranges of the factor m correspond to a different rate-limiting step of the ORR. In particular, the reaction could be limited by 1) the adsorption of oxygen at the gas-cathode interface $O_2^{gas} \leftrightarrow O_2^{ads}$ ($m = 1$); 2) oxygen dissociation $O_2^{ads} \leftrightarrow 2O^{ads}$ ($m = 0.5$); 3) the diffusion processes at the electrode-electrolyte interface ($m = 0.375$); or 4) charge transfer in $O^{ads} + 2e^- + V_O^{\cdot\cdot} \leftrightarrow O_O^x$ ($m = 0.25$), where $V_O^{\cdot\cdot}$ is the oxygen vacancy. In our study (Fig. 7), $m \sim 0.3$ suggests that the electrode-electrolyte interface and the charge transfer are the main limitations to the reaction. For BLFA-5 and BLFA-10, the supply of oxygen vacancies ceases to be the reaction limiting factor at 700 °C. This shows that Ag substitution increases the ionic conductivity, as also suggested by the weakening of the Fe–O bonds calculated by pCOOP (Fig. 3). ASR in BLF + A, on the other hand has a flatter dependence on pO_2, being characterized by m between 0.1 and 0.2. The estimated ECM parameters are reported in Tables S1–S4, where the DRT-like analysis shows that the increasing T and pO_2 lower τ_1 and τ_2, see Fig. 8. We then compared BLFA-5, BLFA-10, and BLF + A against BLF, at the same conditions of T and pO_2, see Table 5, where the EIS fits and corresponding DRT are reported in Figs. S6–S13. We observed that, for BLFA-5 and BLFA-10, the resistances and the relaxation time constants were lower, indicating a beneficial role of Ag substitution on the ORR. Conversely, while BLF + A has a reduced resistance, it led to higher relaxation time constants.

3.5. Electrical conductivity

The electrical conductivity of BLF is mainly of p-type, where the charge is transferred via the transport of the electron holes in the oxygen sublattice. As is typical in semiconductors, the conductivity increases with temperature as long as the number of oxygen vacancies is constant. On the other hand, temperatures above 300 °C generate a sharp increase of the number of oxygen vacancies.[13] This causes a reduction of the number of holes, which are the major charge carriers of p-type conductivity. Therefore, the conductivity peaks at temperatures ranging between 350 °C and 450 °C, and then starts to decline. This is apparent in Fig. 9b for all the materials studied. In this framework, we study how Ag metal and Ag substitution influence conductivity. Firstly, comparing BLF and BLF + A, we can observe the influence of the Ag metal secondary phase. The temperature dependence of the conductivity curve of BLF + A is very similar to the one of BLF, but higher and shifted to the left. This suggests that the conductivity improvement in BLF + A is due to the high electron-driven metallic conduction through the Ag metal secondary phase. The left shift may be due to the negative correlation between metallic conductivity and temperature. The sample BLFA-5 is mainly affected by the presence of $Ag^{+/3+}$ in the lattice, which causes a higher number of oxygen vacancies and a lower number of holes. This reduction of the charge carriers was also suggested by the computational Bader charge study (Fig. 2) and causes a lower electronic conductivity. Finally, the BLFA-10 sample shows an intermediate behavior. As in BLFA-5, the presence of $Ag^{+/3+}$ in the lattice lowers its conductivity, but the presence of the Ag metal secondary phase makes it higher than BLFA-5 and generates a left-shift of its conductivity peak.

3.6. Electrical conductivity relaxation

The dual effect of the Ag introduction observed in the electrical conductivity is reflected in the ECR response, see Fig. 9c and Fig. S14. Taking the BLF case as a starting point, we find that the presence of Ag metal in BLF + A hinders oxygen incorporation, resulting in the slowest
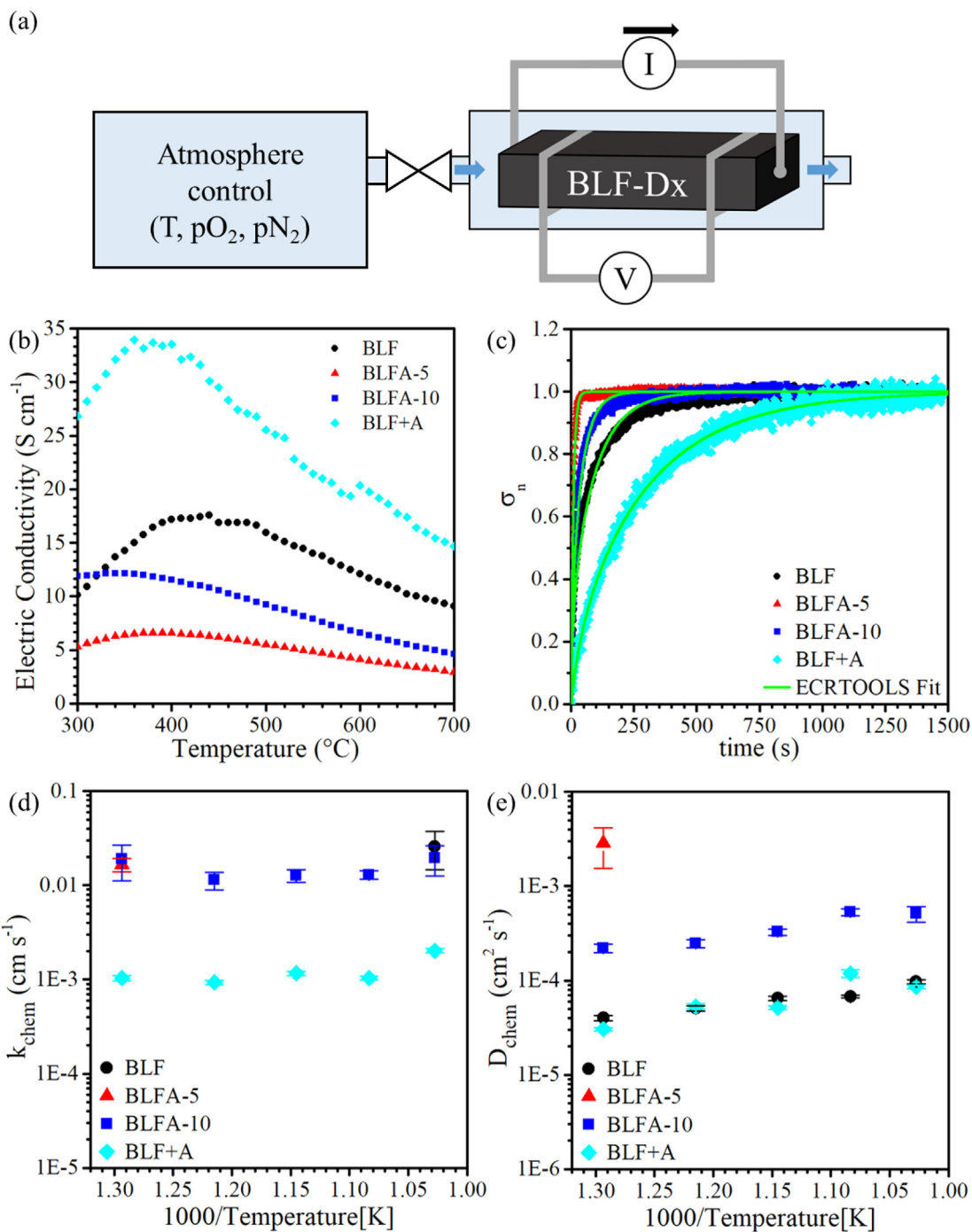
Fig. 9. (a) Schematics of the 4-probe method used for measuring the electrical conductivity and ECR. (b) Electrical conductivities of BLF, BLFA-5, BLFA-10, and BLF + A pO_2 = 21%. (c) Representative ECR responses with a pO_2 step from 50% to 21%, conducted at $T = 500\,°C$; the corresponding ECRTOOLS fits are also shown. (d)k_{chem} and (e) D_{chem} obtained by ECR regression after a pO_2 step change from 50% to 21%. Due to the fast kinetics, the coefficients for BLFA-5 at high temperatures could not be obtained reliably.

response. This observation confirms our initial hypothesis on BLF + A's EIS arc reduction, suggesting that it should not be attributed to a fast oxygen incorporation but only to an improved electronic stabilization of the cathode-electrolyte interface. Still in Fig. 9c, the material with the fastest response is BLFA-5, which is boosted by Ag substitution, but not hindered by the Ag metal. Finally, the response of BLFA-10 is slower than that of BLFA-5 due to the presence of the Ag metal secondary phase. These results are not in contrast with the EIS. Indeed, Ag metal has a positive effect on the EIS by aiding the electronic stabilization at the cathode-electrolyte interface. However, it has a negative effect on the

ECR. Yet Ag-substitution also improves the ECR by increasing the number of oxygen vacancies in the perovskite. The constants k_{chem} and D_{chem} fitted with ECRTOOLS are shown in Fig. 9d and e. The fitting result suggests that the mere introduction of Ag metal particles lowers k_{chem}, while D_{chem} is boosted by the Ag substitution in the lattice. Fitting these parameters on a thick sample is non-trivial, and may lead to some mismatches. In particular, for BLF, the slow kinetics of D_{chem} results in a non-fittable k_{chem}. On the other hand, for BLFA-5, the fast kinetics of the material at high temperatures causes a poor fit and large error bars.

4. Conclusions

This study has helped to elucidate the influence of Ag introduction in the BFO-derived series of materials BLFA-x. We first carried out a computational study on Ag-doped BFO, to predict the effects of Ag substitution in BFO. Then, to experimentally distinguish the influence of Ag substitution from the one of the Ag metal as a secondary phase, we compared the BLFA-x series with BLF + A. We observed that both Ag substitution and Ag metal phase contribute to the enhancement of the ORR catalysis in different ways. Cationic substitution of Ag increases the number of oxygen vacancies in the material, improving in this way the catalytic performances for ORR. However, Ag substitution reduces the electronic conductivity, since it lowers the number of holes. On the other hand, the electronic conductivity is boosted by the presence of the Ag metal phase, which also stabilizes the charge distribution at the cathode-electrolyte interface. We believe that such properties make Ag an interesting element to use in tuning SOFC materials and an opportunity for IT-SOFC cathode development.

Declaration of competing interest

The authors declare no conflict of interest.

Acknowledgments

Appendix A. Supplementary data

Supplementary data to this article can be found online at https://doi.org/10.1016/j.matre.2021.100018.

References

1. Chu S, Majumdar A. Opportunities and challenges for a sustainable energy future. *Nature*. 2012;488:294.
2. Stolten D, Samsun RC, Garland N. *Fuel Cells: Data, Facts, and Figures*. John Wiley & Sons; 2016.
3. Wachsman ED, Lee KT. Lowering the temperature of solid oxide fuel cells. *Science*. 2011;334:935–939.
4. Brett DJ, Atkinson A, Brandon NP, Skinner SJ. Intermediate temperature solid oxide fuel cells. *Chem Soc Rev*. 2008;37:1568–1578.
5. Dong F, Chen Y, Chen D, Shao Z. Surprisingly high activity for oxygen reduction reaction of selected oxides lacking long oxygen-ion diffusion paths at intermediate temperatures: a case study of cobalt-free $BaFeO_{3-\delta}$. *ACS Appl Mater Interfaces*. 2014;6:11180–11189.
6. Xu D, Dong F, Chen Y, et al. Cobalt-free niobium-doped barium ferrite as potential materials of dense ceramic membranes for oxygen separation. *J Membr Sci*. 2014;455:75–82.
7. Dong F, Chen D, Chen Y, Zhao Q, Shao Z. La-doped $BaFeO_{3-\delta}$ perovskite as a cobalt-free oxygen reduction electrode for solid oxide fuel cells with oxygen-ion conducting electrolyte. *J Mater Chem*. 2012;22:15071–15079.
8. Kida T, Takauchi D, Watanabe K, et al. Oxygen permeation properties of partially A-site substituted $BaFeO_{3-\delta}$ perovskites. *J Electrochem Soc*. 2009;156. E187-E91.
9. Ding X, Gao X, Zhu W, Wang J, Jiang J. Electrode redox properties of $Ba_{1-x}La_xFeO_{3-\delta}$ as cobalt free cathode materials for intermediate-temperature SOFCs. *Int J Hydrogen Energy*. 2014;39:12092–12100.
10. Liu J, Wang J, Belotti A, Ciucci F. P-substituted $Ba_{0.95}La_{0.05}FeO_{3-\delta}$ as a cathode material for SOFCs. *ACS Appl Energy Mater*. 2019;2(8):5472–5480. https://doi.org/10.1021/acsaem.9b00624.
11. Zhou W, Ran R, Shao Z. Progress in understanding and development of $Ba_{0.5}Sr_{0.5}Co_{0.8}Fe_{0.2}O_{3-\delta}$-based cathodes for intermediate-temperature solid-oxide fuel cells: a review. *J Power Sources*. 2009;192:231–246.
12. Aschauer U, Pfenninger R, Selbach SM, Grande T, Spaldin NA. Strain-controlled oxygen vacancy formation and ordering in $CaMnO_3$. *Phys Rev B*. 2013;88, 054111.
13. Wang J, Saccoccio M, Chen D, Gao Y, Chen C, Ciucci F. The effect of A-site and B-site substitution on $BaFeO_{3-\delta}$: an investigation as a cathode material for intermediate-temperature solid oxide fuel cells. *J Power Sources*. 2015;297:511–518.
14. Wang J, Lam KY, Saccoccio M, Gao Y, Chen D, Ciucci F. Ca and in co-doped $BaFeO_{3-\delta}$ as a cobalt-free cathode material for intermediate-temperature solid oxide fuel cells. *J Power Sources*. 2016;324:224–232.
15. Zhu X, Wang H, Yang W. Structural stability and oxygen permeability of cerium lightly doped $BaFeO_{3-\delta}$ ceramic membranes. *Solid State Ionics*. 2006;177:2917–2921.
16. Shannon RD. Revised effective ionic radii and systematic studies of interatomic distances in halides and chalcogenides. *Acta Crystallogr Sect A Cryst Phys Diffr Theor Gen Crystallogr*. 1976;32:751–767.
17. Zhang Z, Xu X, Zhang J, et al. Silver-doped strontium niobium cobaltite as a new perovskite-type ceramic membrane for oxygen separation. *J Membr Sci*. 2018;563:617–624.
18. Lim E, Kim YJ, Kim JH, et al. NO oxidation activity of Ag-doped perovskite catalysts. *J Catal*. 2014;319:182–193.
19. Kucharczyk B, Adamska K, Tylus W, Miśta W, Szczygieł B, Winiarski J. Effect of silver addition to $LaFeO_3$ perovskite on the activity of monolithic $La_{1-x}Ag_xFeO_3$ perovskite catalysts in methane hexane oxidation. *Catal Lett*. 2019;149:1919–1933.
20. Guo S, Wu H, Puleo F, Liotta LF. B-site metal (Pd, Pt, Ag, Cu, Zn, Ni) promoted $La_{1-x}Sr_xCo_{1-y}Fe_yO_{3-\delta}$ perovskite oxides as cathodes for IT-SOFCs. *Catalysts*. 2015;5:366–391.
21. Zhu Y, Zhou W, Ran R, Chen Y, Shao Z, Liu M. Promotion of oxygen reduction by exsolved silver nanoparticles on a perovskite scaffold for low-temperature solid oxide fuel cells. *Nano Lett*. 2015;16:512–518.
22. Kim J, Kim J, Seo H, et al. Ex-solved Ag nanocatalysts on a Sr-free parent scaffold authorize a highly efficient route of oxygen reduction. *Adv Funct Mater*. 2020:2001326.
23. Kresse G, Furthmüller J. Efficiency of ab-initio total energy calculations for metals and semiconductors using a plane-wave basis set. *Comput Mater Sci*. 1996;6:15–50.
24. Kresse G, Furthmüller J. Efficient iterative schemes for ab initio total-energy calculations using a plane-wave basis set. *Phys Rev B*. 1996;54:11169.
25. Blöchl PE. Projector augmented-wave method. *Phys Rev B*. 1994;50:17953.
26. Perdew JP, Burke K, Ernzerhof M. Generalized gradient approximation made simple. *Phys Rev Lett*. 1996;77:3865.
27. Anisimov VI, Aryasetiawan F, Lichtenstein A. First-principles calculations of the electronic structure and spectra of strongly correlated systems: the LDA+ U method. *J Phys Condens Matter*. 1997;9:767.
28. Baiyee ZM, Chen C, Ciucci F. A DFT+U study of A-site and B-site substitution in $BaFeO_{3-\delta}$. *Phys Chem Chem Phys*. 2015;17:23511–23520.
29. Chen C, Ciucci F. Designing Fe-based oxygen catalysts by density functional theory calculations. *Chem Mater*. 2016;28:7058–7065.
30. Chen C, Baiyee ZM, Ciucci F. Unraveling the effect of La A-site substitution on oxygen ion diffusion and oxygen catalysis in perovskite $BaFeO_3$ by data-mining molecular dynamics and density functional theory. *Phys Chem Chem Phys*. 2015;17:24011–24019.
31. Jain A, Ong SP, Hautier G, et al. Commentary: the Materials Project: a materials genome approach to accelerating materials innovation. *Apl Mater*. 2013;1, 011002.
32. Wang L, Maxisch T, Ceder G. Oxidation energies of transition metal oxides within the GGA+ U framework. *Phys Rev B*. 2006;73:195107.
33. Maintz S, Deringer VL, Tchougréeff AL, Dronskowski R. LOBSTER: a tool to extract chemical bonding from plane-wave based DFT. *J Comput Chem*. 2016;37:1030–1035.
34. Maintz S, Deringer VL, Tchougréeff AL, Dronskowski R. Analytic projection from plane-wave and PAW wavefunctions and application to chemical-bonding analysis in solids. *J Comput Chem*. 2013;34:2557–2567.
35. Deringer VL, Tchougréeff AL, Dronskowski R. Crystal orbital Hamilton population (COHP) analysis as projected from plane-wave basis sets. *J Phys Chem*. 2011;115:5461–5466.
36. Nelson R, Ertural C, George J, Deringer VL, Hautier G, Dronskowski R. LOBSTER: local orbital projections, atomic charges, and chemical-bonding analysis from projector-augmented-wave-based density-functional theory. *J Comput Chem*. 2020;41(21):1931–1940.
37. Gao Y, Wang J, Lyu Y-Q, Lam K, Ciucci F. In situ growth of Pt_3Ni nanoparticles on an A-site deficient perovskite with enhanced activity for the oxygen reduction reaction. *J Mater Chem*. 2017;5:6399–6404.
38. Chen D, Wang J, Zhang Z, Shao Z, Ciucci F. Boosting oxygen reduction/evolution reaction activities with layered perovskite catalysts. *Chem Commun*. 2016;52:10739–10742.
39. Hao Y, Shao Z, Mederos J, Lai W, Goodwin DG, Haile SM. Recent advances in single-chamber fuel-cells: experiment and modeling. *Solid State Ionics*. 2006;177:2013–2021.
40. Ciucci F, Chen C. Analysis of electrochemical impedance spectroscopy data using the distribution of relaxation times: a bayesian and hierarchical bayesian approach. *Electrochim Acta*. 2015;167:439–454.
41. Saccoccio M, Wan TH, Chen C, Ciucci F. Optimal regularization in distribution of relaxation times applied to electrochemical impedance spectroscopy: ridge and lasso regression methods-a theoretical and experimental study. *Electrochim Acta*. 2014;147:470–482.
42. Liu J, Ciucci F. The Deep-Prior distribution of relaxation times. *J Electrochem Soc*. 2020;167, 026506.
43. Effat MB, Quattrocchi E, Wan TH, Saccoccio M, Belotti A, Ciucci F. Electrical conductivity relaxation in the nonlinear regime. *J Electrochem Soc*. 2017;164. F1671-F89.
44. Ciucci F. Electrical conductivity relaxation measurements: statistical investigations using sensitivity analysis, optimal experimental design and ECRTOOLS. *Solid State Ionics*. 2013;239:28–40.

45. Suh I-K, Ohta H, Waseda Y. High-temperature thermal expansion of six metallic elements measured by dilatation method and X-ray diffraction. *J Mater Sci*. 1988;23: 757–760.
46. Ferraria AM, Carapeto AP, do Rego AMB. X-ray photoelectron spectroscopy: silver salts revisited. *Vacuum*. 2012;86:1988–1991.
47. Kaspar TC, Droubay T, Chambers SA, Bagus PS. Spectroscopic evidence for Ag (III) in highly oxidized silver films by X-ray photoelectron spectroscopy. *J Phys Chem C*. 2010;114:21562–21571.
48. Mori K, Kamiyama T, Kobayashi H, Itoh K, Otomo T, Ikeda S. Local structure of $BaFeO_{3-\delta}$ studied by neutron scattering. *Phys B Condens Matter*. 2003;329:807–808.
49. Biesinger MC, Payne BP, Grosvenor AP, Lau LW, Gerson AR, Smart RSC. Resolving surface chemical states in XPS analysis of first row transition metals, oxides and hydroxides: Cr, Mn, Fe, Co and Ni. *Appl Surf Sci*. 2011;257:2717–2730.
50. Choi M, Hwang S, Byun D, Lee W. Enhanced charge transfer with Ag grids at electrolyte/electrode interfaces in solid oxide fuel cells. *J Mater Chem*. 2016;4: 4420–4424.
51. Erikson H, Sarapuu A, Tammeveski K. Oxygen reduction reaction on silver catalysts in alkaline media: a minireview. *ChemElectroChem*. 2019;6:73–86.
52. Camaratta M, Wachsman E. Silver–bismuth oxide cathodes for IT-SOFCs; Part I—microstructural instability. *Solid State Ionics*. 2007;178:1242–1247.
53. Escudero M, Aguadero A, Alonso JA, Daza L. A kinetic study of oxygen reduction reaction on La_2NiO_4 cathodes by means of impedance spectroscopy. *J Electroanal Chem*. 2007;611:107–116.
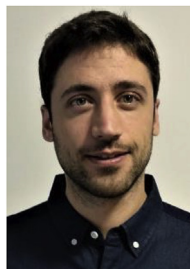
Alessio Belotti is a Ph.D. candidate at The Hong Kong University of Science and Technology under the auspices of the Hong Kong Ph.D. Fellowship Scheme. He graduated with a dual B.Sc. degree at Politecnico di Milano, Italy, and Tongji University, China. Then, he obtained an M.Sc. in Energy Engineering at Politecnico di Milano. After spending some years in the industry, Alessio joined academia in Prof. Ciucci's research group. He conducts experimental and theoretical investigations on advanced materials for electrochemical energy conversion and storage, with a particular focus on solid oxide and proton ceramic fuel cells.

Francesco Ciucci is an Associate Professor at The Hong Kong University of Science and Technology. Francesco graduated *cum laude* from Politecnico di Milano, Italy, and Ecole Centrale Paris, France. After getting his Ph.D. from the California Institute of Technology, USA, he did his postdoctoral work at the University of Heidelberg, Germany. Francesco's current research centers on solid-state energy technologies, including solid-oxide fuel cells, electrolyzers, and solid-state batteries.